Original Paper

Nanoconfined multi-phase interactions govern distinct phase behavior of CO_2-oil in shale during CCUS-EOR process

Yu-Jiao He [a], Bing Wei [a,*], Jun-Yu You [b], Le-Le Wang [a], Xiang Zhang [c], Han-Lin Luo [a],
Valeriy Kadet [d]

[a] *State Key Laboratory of Oil and Gas Reservoir Geology and Exploitation, Southwest Petroleum University, Chengdu, 610500, Sichuan, China*
[b] *School of Petroleum and Natural Gas Engineering, Chongqing University of Science and Technology, Chongqing, 401331, China*
[c] *Department of Energy and Power Engineering, Tsinghua University, Beijing, 100084, China*
[d] *Gubkin Russia State University of Oil and Gas, Moscow, 119991, Russia*

A R T I C L E I N F O

Article history:
Received 23 July 2025
Received in revised form
3 Sept

Nomenclature

a	Attractive parameter in PR-EOS, pa·m^6/mol^2
a_{fp}	Fluid-wall interaction factor
b	Repulsive parameter in PR-EOS, m^3/mol
$f_{i\mathrm{L}}$	Fugacity of i-th component in liquid phase
$f_{i\mathrm{V}}$	Fugacity of i-th component in vapor phase
L	Length of cylindrical pore, m
k_{ij}	Binary interaction coefficient
MW	Molecular weight, kg/mol
N_{A}	Avogadro constant, 6.022×10^{23} mol^{-1}
N_{c}	Total number of components in the mixture
o	Molecular weight-related parameters
p	Reservoir pressure, Pa
p_{c}	Critical pressure of bulk fluid, Pa
p_{cn}	Critical pressure of nanoconfined fluid, Pa
p_{cap}	Capillary pressure, Pa
p_{L}	Pressures of liquid phase, Pa
p_{V}	Pressures of vapor phase, Pa
P_i	Parachor of the i-th component
q	Molecular weight-related parameters
R	Gas constant, 8.314 J/(mol·K)
r_{p}	Pore radius, m
T	Reservoir temperature, K
T_{c}	Critical temperature of bulk fluid, K
T_{cn}	Critical temperature of nanoconfined fluid, K
T_{r}	Reduced temperature
V	Vapor fraction
V_{a}	Adsorbed fluid volume, m^3
V_{e}	Effective volume of a single fluid molecule, m^3
V_{f}	Free fluid volume, m^3
V_{m}	Mole volume, m^3/mol
V_{p}	Total pore volume, m^3
V_{real}	Real volume of a single molecule, m^3
x_i	Mole fraction in liquid phase
y_j	Mole fraction in vapor phase
Z_{L}	Compressibility factor of liquid phase
Z_{V}	Compressibility factor of vapor phase
z_i	Mole fraction of the i-th component in the mixture
Δp^*	Shift of critical pressure
ΔT^*	Shift of critical temperature
δ_{ab}	Adsorption layer thickness, m
θ	Vapor-liquid contact angle, °
$\bar{\rho}$	Molar density, mol/m^3
σ	Interfacial tension, N/m
σ_{LJ}	Lennard-Jones size parameter, m
ω	Acentric factor

Tao et al., 2025), molecular dynamics simulations (MDS) (Dong et al., 2022), density functional theory (DFT) (Li et al., 2014), and equation of state (EOS) (Rui et al., 2025; Yang et al., 2020) models. Experimental methods mainly use nanofluidics to develop lab-on-chip (Bocquet and Tabeling, 2014; Zhong et al., 2020). Wang et al. (2024) measured the minimum miscibility pressure (MMP) of nanoconfined CO_2-shale oil system and observed that miscibility occurred at a pressure lower than that in bulk. Although nanofluidic technique is visually intuitive and relatively mature, it remains challenging to accurately characterize fluid transport behavior in pores smaller than 100 nm, especially below 20 nm. Consequently, nanoconfined fluid phase behavior is primarily investigated through MDS and theoretical approaches (Cai et al., 2024). By using MDS, Vishnyakov et al. (2001) found that the critical temperature of CH_4 decreases significantly with decreasing pore size. Ingebrigtsen and Dyre (2014) also reported enhanced fluid-wall interactions in nanopores, resulting in increased fluid density near the pore walls. DFT is another effective tool for analyzing non-uniform fluid systems and has been applied to study fluid phase transitions under nanoconfinement. Li et al. (2014) investigated the adsorption phase behavior of pure and mixed components in carbon slit nanopores, demonstrating that DFT is capable of handling complex pore structures. The above methods, however, are computationally expensive and challenging to apply in complex multicomponent systems. Moreover, MDS is not competent for field-scale reservoir simulations. To address these limitations, EOS models have been widely used to simulate the phase behavior of bulk fluids owing to their solid theoretical foundation, high computational efficiency, and ease of engineering implementation. In 1976, Peng and Robinson developed the Peng-Robinson equation of state (PR-EOS) (Peng and Robinson, 1976) to account for the effects of temperature, molar volume, intermolecular attraction, and critical properties. The PR-EOS has been widely employed to calculate the thermodynamic properties and vapor-liquid equilibrium (VLE) of various pure substances and mixtures in bulk. However, the deviations caused by nanoconfinement render the traditional PR-EOS inappropriate for studying phase behavior in shale. Both the shift in critical properties and the vapor-liquid phase pressure difference caused by capillary pressure are well-recognized effects incorporated into studies of nanoconfined fluid phase behavior. To quantify the critical property shifts in confined spaces, Zarragoicoechea and Kuz (2004) established a quadratic relationship between the critical properties of Lennard-Jones fluids and the dimensionless pore size. This relationship has been commonly adopted in subsequent studies. Considering the influence of capillary pressure, Zhang et al. (2017) incorporated it into VLE calculation. They found that when pore sizes fall below 50 nm, capillary pressure significantly reduces the bubble point pressure and MMP of CO_2-oil systems. Teklu et al. (2014) observed significant reductions in bubble point pressure, dew point pressure, interfacial tension (IFT), and MMP, alongside an increase in upper dew point pressure. Wei et al. (2022) calculated the IFT between crude oil and CH_4 and predicted MMP in micro- and nanopores. They reported that when pore radius falls below 100 nm, both IFT and MMP decrease significantly, with MMP reductions up to 38.8%. As the pore radius decreases, the reduced distance between fluid molecules and pore walls enhances fluid-wall interactions and affects intermolecular attractions (Dong et al., 2022; Yang et al., 2019, 2020). To capture these effects, Yang et al. (2019) modified the PR-EOS by introducing a fluid-wall interaction term. They established correlations for critical property shifts and integrated capillary pressure into VLE calculations. Subsequently, they further adjusted the attraction and co-volume terms in PR-EOS to account for the combined effects (Yang et al., 2020). The results showed that nanoconfinement narrows the two-phase region of CO_2-oil system, lowers MMP and enhances miscible flooding recovery. However, most studies on capillary pressure assume a single wettability condition, whereas actual reservoirs often exhibit mixed-wet characteristics. To explore wettability effects on confined phase behavior, Feng et al. (2021) extended PR-EOS by incorporating fluid-wall interactions and wettability. Their study showed that in 10 nm oil-wet pores, bubble point pressure and IFT drop to about 1/6 and 1/9, respectively, of values under intermediate wettability conditions. These findings demonstrate strong wettability dependence in nanoconfined fluid. Another nanoconfinement manifestation is fluid adsorption (Li et al., 2021; Zhang et al., 2019). It leads to uneven fluid distribution, a reduction in free fluid volume, and changes in molar volume. To account for adsorption, Cui et al. (2018) modified the molar volume term in PR-EOS and incorporated capillary pressure into VLE calculation. Their results demonstrated substantial phase envelope alterations for pores smaller than 50 nm. More recently, Lin et al. (2025) empirically modified the m term in the PR-EOS α function to

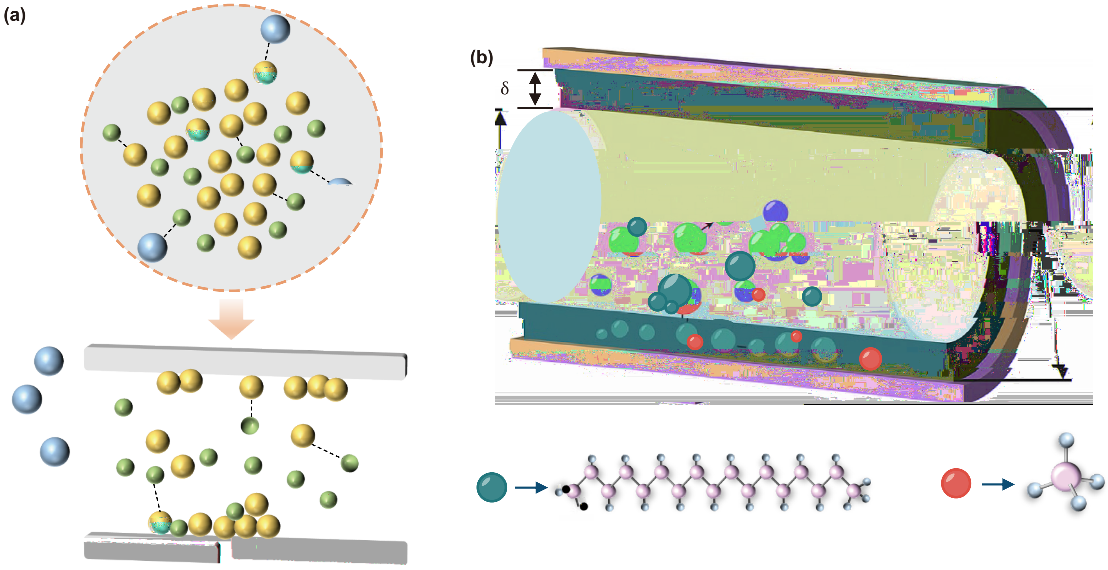

Fig. 1. Nanoconfinement in shale. **(a)** Fluid-wall interactions: molecule size (color spheres) and intermolecular attraction (dashed lines), **(b)** fluid adsorption.

$$\varepsilon=\frac{V_e}{V_{\text{real}}} \tag{17}$$

The total number of fluid molecules (N_t) and adsorbed fluid molecules (N_a) within the pore are determined using Eqs. (7)–(13):

$$N_t=\frac{V_p}{V_{et}}=\frac{\pi {r_p}^2 L}{\varepsilon_t V_{\text{real}}} \tag{18}$$

$$N_a=\frac{V_a}{V_{ea}}=\frac{\pi {r_p}^2 L-\pi\left(r_p-\delta_{ab}\right)^2 L}{\varepsilon_a V_{\text{real}}} \tag{19}$$

$$V_{mp}=\frac{V_p}{\left(N_t-N_a\right)/N_A}=\frac{N_t}{N_t-N_a}V_{mb}=\frac{V_m}{1-\frac{\varepsilon_t}{\varepsilon_a}\frac{\delta_{ab}}{{r_p}^2}\left(2r_p-\delta_{ab}\right)}=\lambda V_{mb} \tag{20}$$

where $\lambda=\frac{1}{1-\frac{\varepsilon_t}{\varepsilon_a}\frac{\delta_{ab}}{{r_p}^2}\left(2r_p-\delta_{ab}\right)}$ represent the correction coefficient for the effective molar volume of fluids in nanopores.

2.3. Modified PR-EOS

By thoroughly accounting for fluid-wall interactions and variations in V_m, the PR-EOS is modified as shown in Eq. (21). This formulation provides a more accurate phase behavior prediction in shale.

$$P=\frac{RT}{V_{mp}-b}-\frac{a-a_{fp}}{V_{mp}\left(V_{mp}+b\right)+b\left(V_{mp}-b\right)} \tag{21}$$

To ensure thermodynamic consistency in the modified PR-EOS, the critical point condition requires both the first and second partial derivatives of pressure with respect to V_{mp} to vanish at the critical temperature.

$$\left(\frac{\partial p}{\partial V_{mp}}\right)_{T=T_c}=\left(\frac{\partial^2 p}{\partial V_{mp}^2}\right)_{T=T_c}=0 \tag{22}$$

Based on Eqs. (21) and (22), the expressions for parameters a and b in the modified PR-EOS are derived, with the detailed derivation provided in the Supplementary Information.

$$a=\frac{0.45724R^2T_c^2}{p_c}+a_{fp} \tag{23}$$

$$b=\frac{0.07780RT_c}{p_c\lambda} \tag{24}$$

Accordingly, the critical temperature and pressure of nanoconfined fluid can be determined as follows:

$$T_{cn}=0.1702\frac{a-a_{fp}}{\alpha bR}\lambda \tag{25}$$

$$p_{cn}=0.0132\frac{a-a_{fp}}{\alpha b^2}\lambda^2 \tag{26}$$

For multi-component mixtures, the parameters a_m and b_m in both the vapor and liquid phases are calculated using the van der Waals mixing rules (Rachford and Rice, 1952).

$$a_{mL}=\sum_{i=1}^{N_c}\sum_{j=1}^{N_c}x_i x_j\left(a_i a_j \alpha_i \alpha_j\right)^{0.5}\left(1-k_{ij}\right) \tag{27}$$

$$a_{mV}=\sum_{i=1}^{N_c}\sum_{j=1}^{N_c}y_i y_j\left(a_i a_j \alpha_i \alpha_j\right)^{0.5}\left(1-k_{ij}\right) \tag{28}$$

$$b_{mL}=\sum_{i=1}^{N_c}x_i b_i \tag{29}$$

$$b_{mV}=\sum_{i=1}^{N_c}y_i b_i \tag{30}$$

The compressibility factor forms of the modified PR-EOS for the vapor and liquid phases are given by:

$$\begin{aligned}&Z_L-\left(1-B_L\right)Z_L^3+\left(A_L-A_{fpL}-2B_L-3B_L^2\right)Z_L\\&\quad-\left(A_L B_L-A_{fpL}B_L-B_L^2-B_L^3\right)=0\end{aligned} \tag{31}$$

$$Z_{\mathrm{V}}-(1-B_{\mathrm{V}})Z_{\mathrm{V}}^{3}+\left(A_{\mathrm{V}}-A_{\mathrm{fpV}}-2B_{\mathrm{V}}-3B_{\mathrm{V}}^{2}\right)Z_{\mathrm{V}}-\left(A_{\mathrm{V}}B_{\mathrm{V}}-A_{\mathrm{fpV}}B_{\mathrm{V}}-B_{\mathrm{V}}^{2}-B_{\mathrm{V}}^{3}\right)=0 \tag{32}$$

where $A_{\mathrm{L}}=\frac{a_{\mathrm{mL}}p_{\mathrm{L}}}{(RT)^{2}}$, $A_{\mathrm{V}}=\frac{a_{\mathrm{mV}}p_{\mathrm{V}}}{(RT)^{2}}$, $B_{\mathrm{L}}=\frac{b_{\mathrm{mL}}p_{\mathrm{L}}}{RT^{2}}$, $B_{\mathrm{V}}=\frac{b_{\mathrm{mV}}p_{\mathrm{V}}}{RT}$, $A_{\mathrm{fpL}}=\frac{a_{\mathrm{fpmL}}p_{\mathrm{L}}}{(RT)^{2}}$, and $A_{\mathrm{fpV}}=\frac{a_{\mathrm{fpmV}}p_{\mathrm{V}}}{(RT)^{2}}$.

The calculations of vapor and liquid fugacity are as follow:

$$\ln\left(\frac{f_{i\mathrm{L}}}{x_{i}p_{\mathrm{L}}}\right)=\frac{b_{i}}{b_{m\mathrm{L}}}(Z_{\mathrm{L}}-1)-\ln(Z_{\mathrm{L}}-B_{\mathrm{L}})-\frac{A_{\mathrm{L}}-A_{\mathrm{fpL}}}{2\sqrt{2}B_{\mathrm{L}}}\left(\frac{2\varphi_{j\mathrm{L}}}{a_{m\mathrm{L}}}-\frac{b_{i}}{b_{m\mathrm{L}}}\right)\ln\left(\frac{Z_{\mathrm{L}}+2.414B_{\mathrm{L}}}{Z_{\mathrm{L}}-0.414B_{\mathrm{L}}}\right) \tag{33}$$

$$\ln\left(\frac{f_{i\mathrm{V}}}{y_{i}p_{\mathrm{V}}}\right)=\frac{b_{i}}{b_{m\mathrm{v}}}(Z_{\mathrm{V}}-1)-\ln(Z_{\mathrm{V}}-B_{\mathrm{V}})-\frac{A_{\mathrm{V}}-A_{\mathrm{fpV}}}{2\sqrt{2}B_{\mathrm{V}}}\left(\frac{2\varphi_{j\mathrm{V}}}{a_{m\mathrm{V}}}-\frac{b_{i}}{b_{m\mathrm{V}}}\right)\ln\left(\frac{Z_{\mathrm{V}}+2.414B_{\mathrm{V}}}{Z_{\mathrm{V}}-0.414B_{\mathrm{V}}}\right) \tag{34}$$

where $\varphi_{j\mathrm{L}}=\sum_{j=1}^{N_{\mathrm{c}}}x_{i}\left(a_{i}a_{j}\alpha_{i}\alpha_{j}\right)^{0.5}$, and $\varphi_{j\mathrm{V}}=\sum_{j=1}^{N_{\mathrm{c}}}y_{i}\left(a_{i}a_{j}\alpha_{i}\alpha_{j}\right)^{0.5}$.

2.4. Critical properties shift model

Due to the nanoconfining effect, the critical properties of fluids within nanopores differ from those in the bulk phase. The shifts in critical temperature and pressure are calculated using Eqs. (35) and (36):

$$\Delta T^{*}=\frac{T_{\mathrm{c}}-T_{\mathrm{cn}}}{T_{\mathrm{c}}}=\lambda\left(\frac{a_{\mathrm{fp}}}{a}-1\right)+1 \tag{35}$$

$$\Delta p^{*}=\frac{T_{\mathrm{c}}-T_{\mathrm{cn}}}{T_{\mathrm{c}}}=\lambda^{2}\left(\frac{a_{\mathrm{fp}}}{a}-1\right)+1 \tag{36}$$

When $\lambda=1$, the modified PR-EOS reduces to the form without fluid adsorption. When $a_{\mathrm{fp}}=0$, it indicates the absence of fluid-wall interactions. When both conditions are met, the model reverts to the traditional PR-EOS. Based on the generalized van der Waals theory and experimental critical property data, Zarragoicoechea and Kuz (2004) proposed a quadratic relationship between the critical temperature and pressure of Lennard-Jones fluids and the dimensionless pore size. This relationship has been widely adopted in subsequent studies. However, it assumes equal shifts in the critical temperature and pressure. When directly applied to Eqs. (35) and (36), this assumption may yield $T_{\mathrm{cn}}=p_{\mathrm{cn}}=0$, except in two special cases (i.e., $\lambda=1$ and $a_{\mathrm{fp}}=0$). This result contradicts fundamental thermodynamic principles. A new model is therefore required to accurately characterize nanoconfined critical property shifts and enable pressure correction while ensuring mathematical consistency and physical validity. Building on previous research (Pitakbunkate et al., 2016; Singh and Singh, 2011; Tan et al., 2019; Yang et al., 2022; Zhang et al., 2019), critical temperature and pressure data for various pure substances under confinement were systematically collected. To account for molecular size differences, a dimensionless pore radius parameter, $\sigma_{\mathrm{LJ}}/r_{\mathrm{p}}$, was introduced, and all data were fitted using a unified approach.

Fig. 2 presents the exponential dependence of critical temperature and pressure shifts on $\sigma_{\mathrm{LJ}}/r_{\mathrm{p}}$, with correlation coefficients of 0.92 and 0.93, respectively. The corresponding fitting equations are given as follows:

$$\Delta T_{\mathrm{c}}^{*}=\frac{T_{\mathrm{cb}}-T_{\mathrm{cn}}}{T_{\mathrm{cb}}}=0.6757\frac{\sigma_{\mathrm{LJ}}}{r_{\mathrm{p}}}^{0.8377} \tag{37}$$

$$\Delta p_{\mathrm{c}}^{*}=\frac{p_{\mathrm{cb}}-p_{\mathrm{cn}}}{p_{\mathrm{cb}}}=0.9749\frac{\sigma_{\mathrm{LJ}}}{r_{\mathrm{p}}}^{0.6836} \tag{38}$$

The expressions for λ and a_{fp} as functions of $\sigma_{\mathrm{LJ}}/r_{\mathrm{p}}$ are given as follows:

$$\lambda=\frac{0.9749\left(\sigma_{\mathrm{LJ}}/r_{\mathrm{p}}\right)^{0.6836}-1}{0.6757\left(\sigma_{\mathrm{LJ}}/r_{\mathrm{p}}\right)^{0.8377}-1} \tag{39}$$

$$a_{\mathrm{fp}}=\left(\frac{\left[0.6757\left(\sigma_{\mathrm{LJ}}/r_{\mathrm{p}}\right)^{0.8377}-1\right]^{2}}{0.9749\left(\sigma_{\mathrm{LJ}}/r_{\mathrm{p}}\right)^{0.6836}-1}+1\right)a \tag{40}$$

2.5. Vapor-liquid equilibrium calculation

VLE calculation aims to determine the mole fractions of each component in the gas and liquid phases under specified thermodynamic equilibrium conditions. In nanopores, the pronounced curvature of the gas-liquid interface induces significant capillary pressure, resulting in a pressure difference between the gas and liquid phases. This deviates from the isobaric equilibrium assumption commonly applied in conventional reservoirs. Therefore, capillary pressure must be incorporated in nano-confined VLE calculations. The relationship between gas and liquid phase pressures and capillary pressure is expressed as follows:

$$p_{\mathrm{cap}}=p_{\mathrm{V}}-p_{\mathrm{L}} \tag{41}$$

The capillary pressure is calculated by Young-Laplace (Adamson and Gast, 1967) equation:

$$p_{\mathrm{cap}}=\frac{2\sigma\cos\theta}{r_{\mathrm{p}}} \tag{42}$$

IFT is calculated by Parachor (Weinaug and Katz, 1943) model:

$$\sigma=\left[\sum_{i=1}^{N_{\mathrm{c}}}\left(\overline{\rho_{\mathrm{L}}}P_{i}x_{i}-\overline{\rho_{\mathrm{V}}}P_{i}y_{i}\right)\right]^{4} \tag{43}$$

$$P_{i}=(8.12307+1.97473\omega_{i})T_{ci}^{1.03406}p_{ci}^{-0.82636} \tag{44}$$

For multi-component mixtures, vapor-liquid equilibrium is achieved when the chemical potential of each component is equal in both phases, meaning their fugacities are identical. Under such conditions, the VLE relationship can be expressed as:

$$f_{i\mathrm{L}}=f_{i\mathrm{V}},\ i=1,\cdots,N_{\mathrm{c}} \tag{45}$$

The equilibrium constant (K_{i}) is defined as the ratio of the molar fraction of the component i in the vapor phase (y_{i}) to that in the liquid phase (x_{i}). Its initial value is calculated using the Wilson equation (Wilson, 1969):

$$K_{i}=\frac{p_{ci}}{p}\exp\left[5.37(1+\omega_{i})\left(1-\frac{T_{ci}}{T}\right)\right] \tag{46}$$

x_{i} and y_{i} are calculated using the Rachford-Rice (Rachford and Rice, 1952) equation:

$$\sum_{i=1}^{N_{\mathrm{c}}}\frac{z_{i}(K_{i}-1)}{1+(K_{i}-1)V}=0 \tag{47}$$

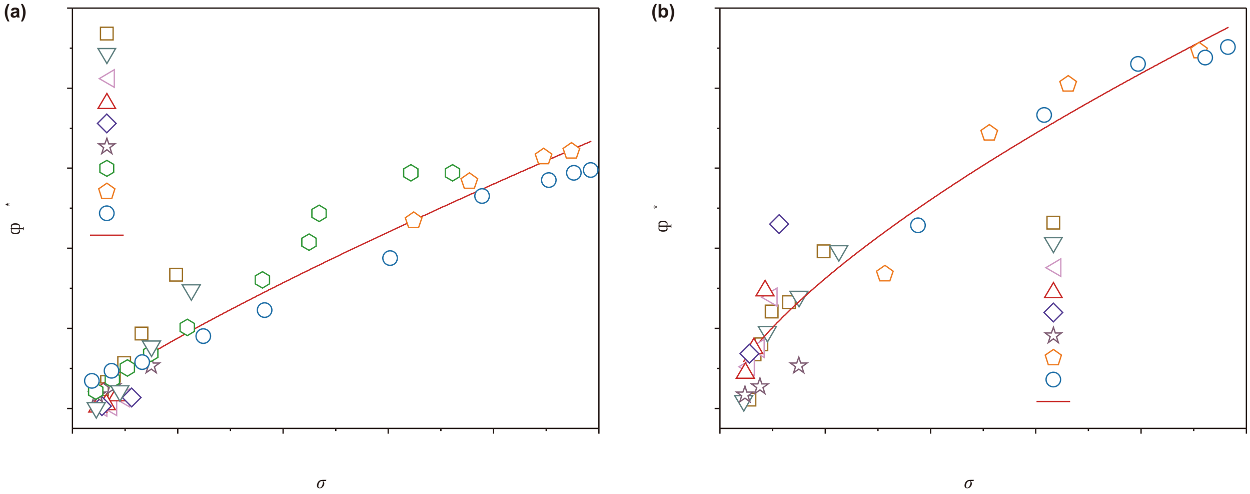

2.6. Proposed model for calculating phase behavior

The computational model for fluid phase behavior in nano-confined spaces is illustrated in Fig. 3. It comprehensively incorporates the combined effects of fluid-wall interactions, fluid adsorption, capillary pressure, and hydrocarbon wettability. The modeling procedure involves several key steps, including critical property modification, equilibrium constant determination, flash calculations, modified PR-EOS computations, and phase equilibrium evaluation. The complete algorithm process is outlined in Algorithm 1.

Algorithm 1:

```
Input: $T$ $r$ $T_{i}$ $p_{i}$ $z_i$ $z_i$ $\omega_i$ $k_{ij}$ $\theta$
Output: $p$ $p$ $\rho$
Initialization: $p$ $p$
Stage 1: Calculate pre-defined:
    $z_i = \frac{z_i}{z_i \quad + z_i}$
    $T_{i} = \quad -\Delta T \quad \times T_{i}, \; p_{i} = \quad -\Delta p \quad \times p_{i}$
Stage 2: Calculate liquid density:
    $K_i \quad = \frac{p_{i}}{p} \left[ \quad ( + \omega_i)\left( -\frac{T_{i}}{T} \right) \right]$
if $\sum z_i \times K_i \quad > \quad \sum z_i \; K_i \quad >$ then
    $\sum_{i=}^{N_c} \frac{z_i \; K_i \quad -}{+ \; K_i \quad - \; V} = \quad x_i = \frac{z_i}{+ \; K_i \quad - \; V} \; y_i = x_i K_i$
else
    $V = \quad x_i = z_i \; y_i =$
end
    $\rho_{-} \quad = \frac{\rho}{Z \; RT}, \quad = \sum_{i}^{N} x_{i} \quad {}_{i} \; \rho \; = \rho_{-}$
Stage 3: Calculate special pressure points:
for $j = \quad N$ do
    $K_i = \frac{p_{i}}{p} \left[ \quad ( + \omega_i)\left( -\frac{T_{i}}{T} \right) \right] \quad \left[ \sum_{i=}^{N} \left( \overline{\rho} \; P_i x_i - \overline{\rho} \; P_i y_i \right) \right] \; p \quad = \frac{\sigma \quad \theta}{r}$
    if $| \; - f_i \quad f_i \; | <$ ⁻ then
        if $| \quad | <$ ⁻ then
            return $= p$
        end
        if $| \sum y_i - \; | <$ ⁻ then
            return $p \quad = p$
        end
        if $| \sum x_i - \; | <$ ⁻ then
            return $p \quad = p$
        end
    end
    else
        $p$
    end
end
```

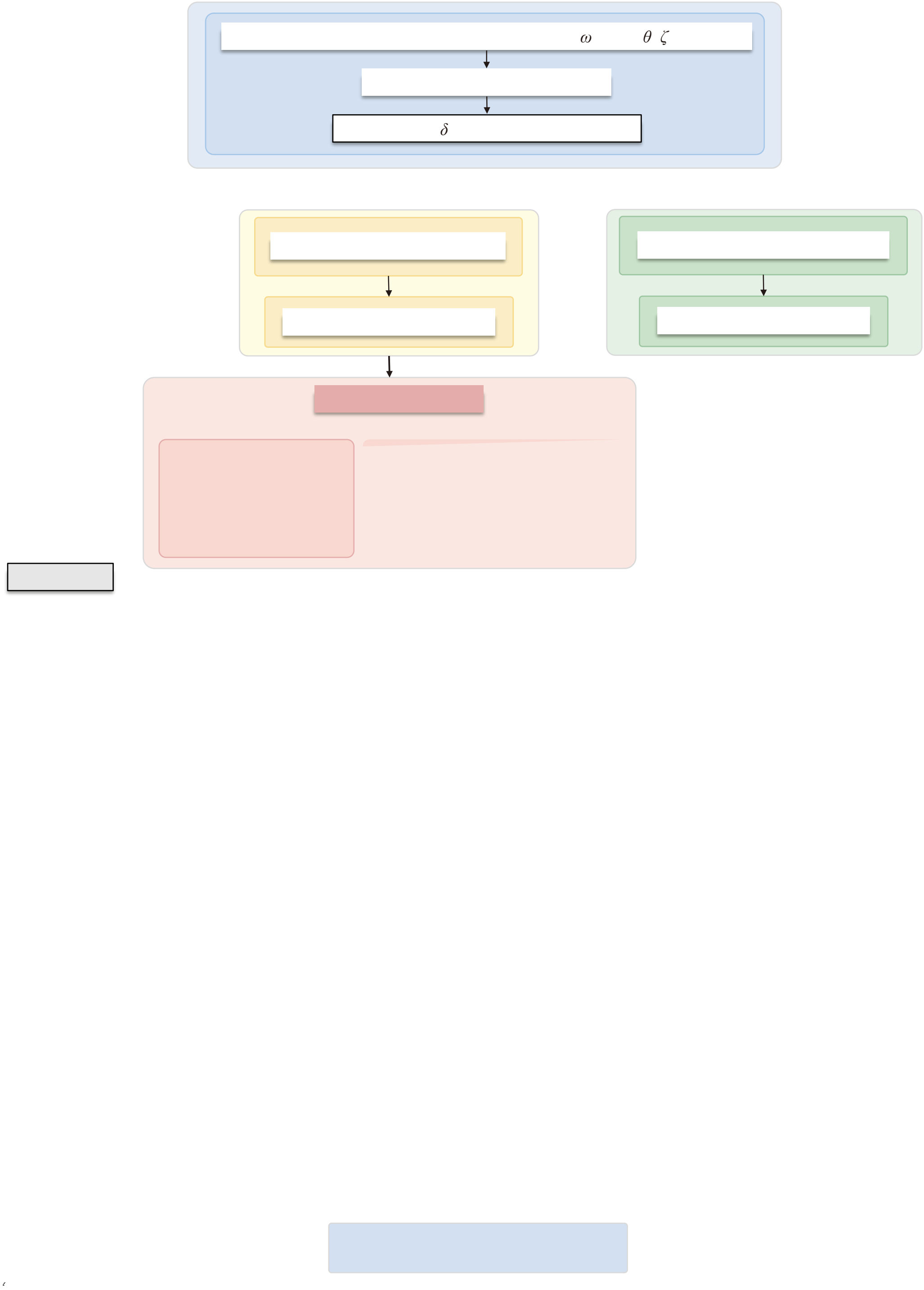

Fig. 3. Proposed computational model for nanoconfined phase behavior analysis of the CO_2-oil in shale.

3. Model validation

To validate the accuracy and generalizability of the proposed model, some available experimental data were collected and employed for analysis, with model predictions systematically compared to experimental results. Tao et al. (2025) measured the MMP of three pure hydrocarbon-CO_2 systems in nanochannels with the depth of 30 nm and 1000 nm at 70 °C using nanofluidics. Simulations under identical conditions are presented in Fig. 4. For the 1000 nm channels, the predicted MMP values closely matched the experimental results, with relative errors ranging from 1.30% to 2.03%, confirming the model's accuracy under bulk conditions. For 30 nm channels, the relative deviations increased to 8.83%–10.65%. This is primarily due to the model's assumption of cylindrical pores, which differs from the rectangular geometry of experimental nanochannels. As reported by Zhao et al. (2024), cylindrical pores tend to exhibit stronger fluid adsorption and fluid-wall interactions compared to slit pores. As a result, the model slightly underestimates the predictions. Nonetheless, given the complexity of fluid behavior at the nanoscale, a deviation of approximately 10% remains reasonable and acceptable. To further evaluate the model's applicability to multi-component systems, nanofluidic experimental data from Cho et al. (2017) were used for comparison. Two mixtures (90% C_8H_{18} + 10% CH_4 and 90% $C_{10}H_{22}$ + 10% CH_4) were tested at 38 °C, as shown in Fig. 5. Under bulk conditions, the deviation between calculated values of p_b and experimental values was below 3.6%, demonstrating the model's adaptability to multicomponent systems. When the pore diameter was reduced to 3.5 nm, the deviation increased to 12.40%–15.30%. This is likely due to the heterogeneous pore size distribution in the experimental chips. In contrast, the model assumes a uniform pore radius, which leads to an underestimation of pore-scale heterogeneity effects.

Since the available experimental data are limited and often employ simplified fluids or do not fully specify wettability, comprehensive validation across all CCUS-EOR scenarios in shale is not yet feasible. Nevertheless, the model's physics-based formulation, which explicitly incorporates key mechanisms (such as fluid-wall interactions, adsorption, capillary pressure, and hydrocarbon wettability), ensures that it captures the essential trends of nanoconfined phase behavior. This foundation enables the model to be applied to a variety of shale reservoirs and fluid systems, providing valuable insights for CCUS-EOR in shale.

4. Results and discussion

4.1. Establishment of fluid model

The shale oil composition and critical properties of each component are listed in Table 1. To reduce computational cost, the oil components were lumped into 7 pseudo-components for multi-phase calculations.

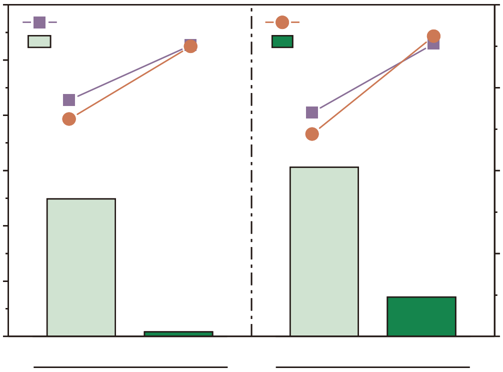

Fig. 5. Comparison between calculated and experimental p_b for 90% C_8H_{18}/10% CH_4 and 90% $C_{10}H_{22}$/10% CH_4 mixtures at 38 °C.

Table 1
Bulk fluid composition and critical properties.

Composition	z_i	T_c, K	p_c, MPa	V_c, L/mol	ω_i	MW, g/mol
N_2	0.0304	126.2	3.350	0.090	0.040	28.01
CO_2	0.0014	304.2	7.280	0.094	0.225	44.01
CH_4	0.4551	190.6	4.540	0.099	0.008	16.04
C_2–C_5	0.0741	42.9	4.155	0.183	0.076	41.92
C_6–C_{10}	0.2665	693.2	3.785	0.575	0.267	101.48
C_{11}–C_{20}	0.1308	805.8	1.262	0.685	0.548	194.01
C_{21}–C_{35}	0.0417	1103.4	0.756	0.830	0.950	361.06

The fluid model parameters were calibrated using experimental data from constant composition expansion and oil swelling tests at 89 °C. These data include the properties such as saturation pressure, gas-oil ratio, viscosity, and density of the shale oil. Adjustable parameters included critical volume, critical pressure, acentric factor, molecular weight, and binary interaction coefficients. The objective was to ensure accurate representation of the reservoir fluid's thermodynamic behavior. The calibrated model successfully reproduces the phase behavior of the target shale oil. Fitting results and binary interaction coefficients are presented in Tables 2 and 3, respectively.

4.2. Nanoconfined phase behavior of CO_2-shale oil

4.2.1. Critical properties shift of different fluids

In nanoconfined spaces, the critical temperature and pressure of fluids deviate significantly from their bulk values. To quantify this effect, critical properties of various fluid components were calculated at different pore radii using the correlations with σ_{LJ}/r_p, as defined in Eqs. (47) and (48). The results are presented in Fig. 6. Notably, the pore radius (r_p) in the equations was corrected to the effective pore radius (r_p-δ_{ab}) to account for the volume occupied by the adsorption layer.

Both critical temperature and pressure decrease with decreasing pore radius, reflecting the nanoconfining effect. When the pore radius exceeds 75 nm, the deviations in critical properties become negligible, and above 100 nm, the values closely approach those of the bulk phase. This trend is consistent with previous studies (Islam et al., 2015; Singh and Singh, 2011; Travalloni et al., 2014). The enhanced confinement is mainly attributed to two factors. First, as the pore radius decreases, fluid molecules are closer to the pore walls, and thus intensifies fluid-wall

Table 2
Fitting results of fluid properties.

Parameter	Measured	Simulated	Error, %
Saturation pressure, MPa	22.00	21.58	1.93
Density, kg/m^3	636.90	650.50	2.13
Viscosity, cp	0.41	0.396	3.38

Table 3
Binary interaction coefficients of pseudo-components.

Composition	CO_2	N_2	CH_4	C_2–C_5	C_6–C_{10}	C_{11}–C_{20}	C_{21}–C_{35}
CO_2	0	0.2000	0	0	0.2047	0	0.0650
N_2	0.2000	0	0	0.2000	0.5000	0.1615	0.1000
CH_4	0	0	0	0.0072	0.0316	0.0635	0.1016
C_2–C_5	0	0.2000	0.0171	0	0.0090	0.0295	0.0584
C_6–C_{10}	0.2047	0.5000	0.0316	0.0090	0	0.0061	0.0227
C_{11}–C_{20}	0	0.1615	0.0635	0.0295	0.0061	0	0.0054
C_{21}–C_{35}							

Fig. 6. Proposed critical properties of fluids for different components in nanopores. **(a)** Critical temperature, **(b)** critical pressure.

interactions. These interactions weaken intermolecular attractions (Yang et al., 2020), leading to phase transitions at lower temperatures and pressures. Second, shale formations are rich in organic matter, which enhances fluid adsorption. With further reduction in pore radius, the proportion of adsorbed molecules increases, effectively narrowing the available pore space. This limits the mobility of alkane molecules (Song et al., 2020; Wang et al., 2015; Zhang et al., 2019), resulting in lower effective molar volume and reducing collision frequency. These effects further suppress phase transitions and amplifies the reduction in critical properties. When the pore radius falls below the molecular scale (approximately 75 nm), the energy states and spatial distributions of fluid molecules significantly change, fundamentally altering the phase behavior.

Fig. 7 follows the same tendency, showing a monotonic decrease in both critical pressure and temperature with decreasing pore radius. Additionally, heavier alkane components with more carbon atoms exhibit more pronounced shifts in critical properties. This is because the larger molecular size limits the number of molecules that can fit within the same pore volume, making their molecular arrangements and interactions more sensitive to confinement (Teklu et al., 2014). A comparison of shifts in Fig. 7 further reveals that critical pressure decreases more significantly than critical temperature for the same component, indicating that critical pressure is particularly sensitive to nanoconfinement.

4.2.2. Saturation pressure

To evaluate the effect of hydrocarbon wettability on phase behavior, saturation pressures of CO_2-oil in shale were calculated at CO_2 fractions of 20 mol% and 40 mol%. Due to the presence of organic matter, shale reservoirs usually exhibit mixed oil-wet and water-wet characteristics. To systematically examine the influence of hydrocarbon wettability on confined phase behavior of CO_2-oil in shale, four contact angles (0°, 45°, 135°, and 180°) were selected. It is important to clarify that the contact angle (θ) here refers to the gas-oil-rock three-phase contact angle, differing from oil-water-rock contact angle. This parameter specifically characterizes the wettability of rock surfaces with respect to shale oil. $\theta = 0^\circ$ represents extreme hydrocarbon wetting, where shale oil fully spreads on the rock surface. In contrast, $\theta = 180^\circ$ indicates extreme hydrocarbon non-wetting, with shale oil forming spherical droplets within the pore space.

To highlight the impact of pore size, a relationship between $1/r_\text{p}$ and saturation pressure was established. Fig. 8 shows a strong linear decrease in saturation pressure with increasing $1/r_\text{p}$ across four wettability conditions, with correlation coefficient (R^2) exceeding 0.989. This confirms that pore size governs saturation pressure and enables the prediction of its variation under different nanoscale conditions. Considering that shale formations usually exhibit intermediate-wet to oil-wet conditions, a contact angle of 45° was selected as the representative case. At 20 mol% of CO_2, the

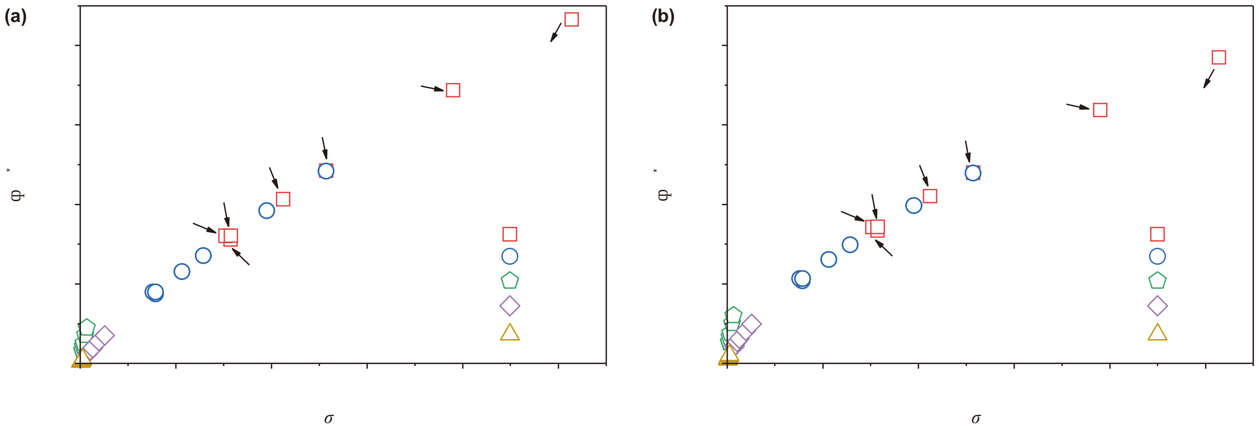

Fig. 7. Relationship between the shifts of critical properties of each component of shale oil under different pore radius and $\sigma_\text{LJ}/r_\text{p}$. **(a)** Shift of critical temperature, **(b)** shift of critical pressure.

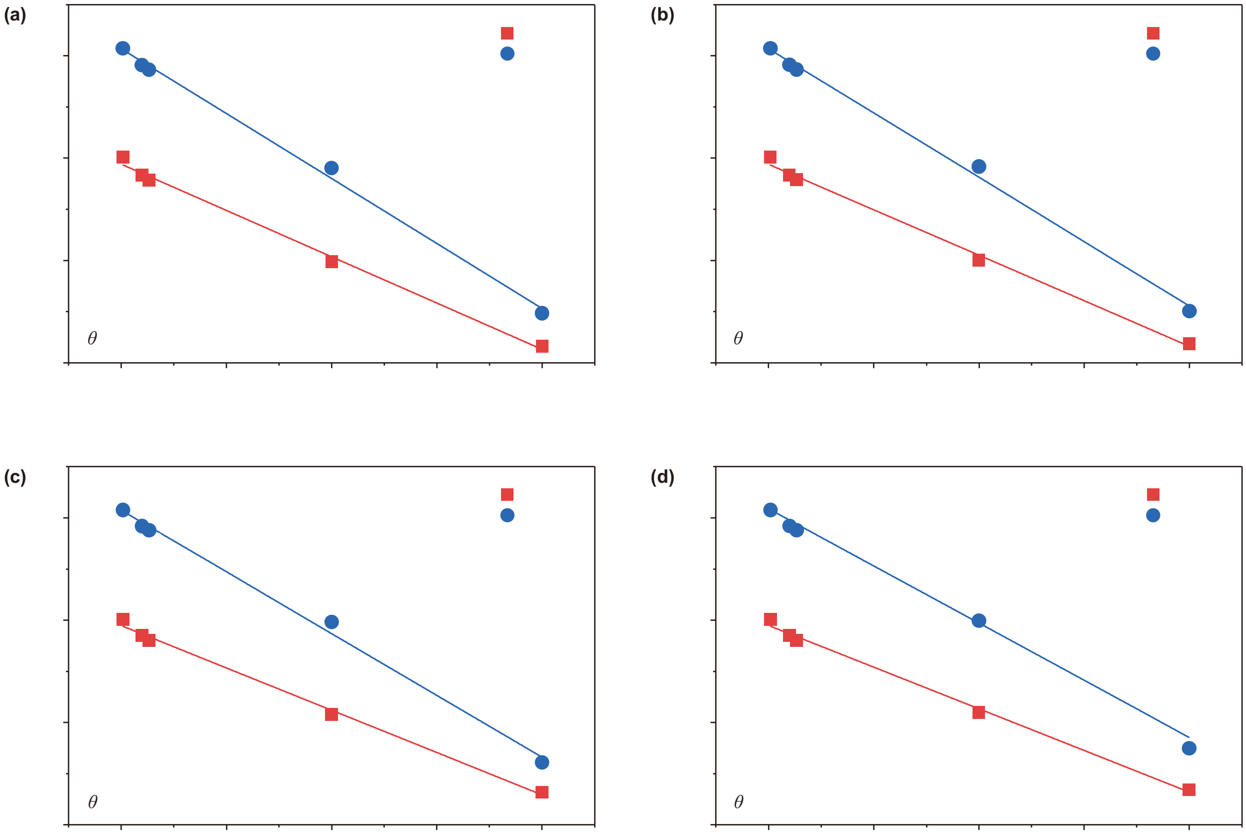

Fig. 8. Variation of saturation pressure with pore size and CO_2 mole fraction under different wettability conditions (θ represents the gas-liquid-rock three-phase contact angle). **(a)** $\theta = 0^{\circ}$

saturation pressure decreases from 25.03 MPa at a pore radius of 1000 nm to 15.79 MPa at 5 nm, representing a 36.92% reduction. In the case of 40 mol% CO_2, it drops from 30.37 MPa to 17.53 MPa, corresponding to a 42.43% decrease. This decline suggests that the confining effects inhibit gas escape from the oil phase and prolong the residence time of light components in liquid phase. As a result, the single-phase liquid region expands, thereby improving fluidity. These findings are consistent with previous results of Teklu et al. (2014) and Du et al. (2020). In addition, Wang et al. (2025) reported that capillary pressure in nanopores significantly enhances mass transfer between gas and liquid phases, particularly by promoting the dissolution of light components into the liquid phase. Thus, the liquid phase becomes enriched with lighter hydrocarbons, improving the compositional stability.

Fig. 9 compares the saturation pressures of different hydrocarbon wettability systems. When the pore radius falls below 100 nm, particularly under 75 nm, the saturation pressure increases as wettability shifts from extreme hydrocarbon wetting ($\theta = 0^{\circ}$) to extreme hydrocarbon non-wetting ($\theta = 180^{\circ}$) and the lowest value is observed at $\theta = 0^{\circ}$. This trend is attributed to the influence of hydrocarbon wettability on capillary pressure (Feng et al., 2021). Under hydrocarbon wetting conditions ($\theta < 90^{\circ}$, $\cos\theta > 0$), the Young-Laplace equation indicates a positive capillary pressure, which effectively suppresses gas phase formation and delays the onset of gas-liquid coexistence. Similarly, the Kelvin equation predicts a reduction in saturation pressure with increasing hydrocarbon wettability. Under hydrocarbon non-wetting conditions ($\theta > 90^\circ$, $\cos\theta < 0$), negative capillary pressure in this case reduces liquid phase stability, making a weaker suppression in bubble point pressure. The relationship between contact angle and capillary pressure further supports this result, as shown in Fig. 10. This effect is particularly pronounced when the pore radius is below 75 nm, while in larger pores, capillary pressure diminishes and the impact of wettability on saturation pressure correspondingly weakens. Moreover, increasing the mole fraction of CO_2 from 20 mol% to 40 mol%, under the same hydrocarbon wettability and pore size conditions, leads to a higher saturation pressure but a lower capillary pressure. This is primarily due to the enhanced solubility of CO_2 in shale oil, which reduces the density difference and IFT between the gas and liquid phases. Thus, although a higher CO_2 fraction promotes gas dissolution and raises saturation pressure, the resulting decrease in IFT subsequently diminishes the capillary pressure.

4.2.3. Oil density

This work further investigates how the average density of the free oil phase within nanopores varies with pore size and hydrocarbon wettability under two distinct pressures (10 MPa, 40 MPa). The wr

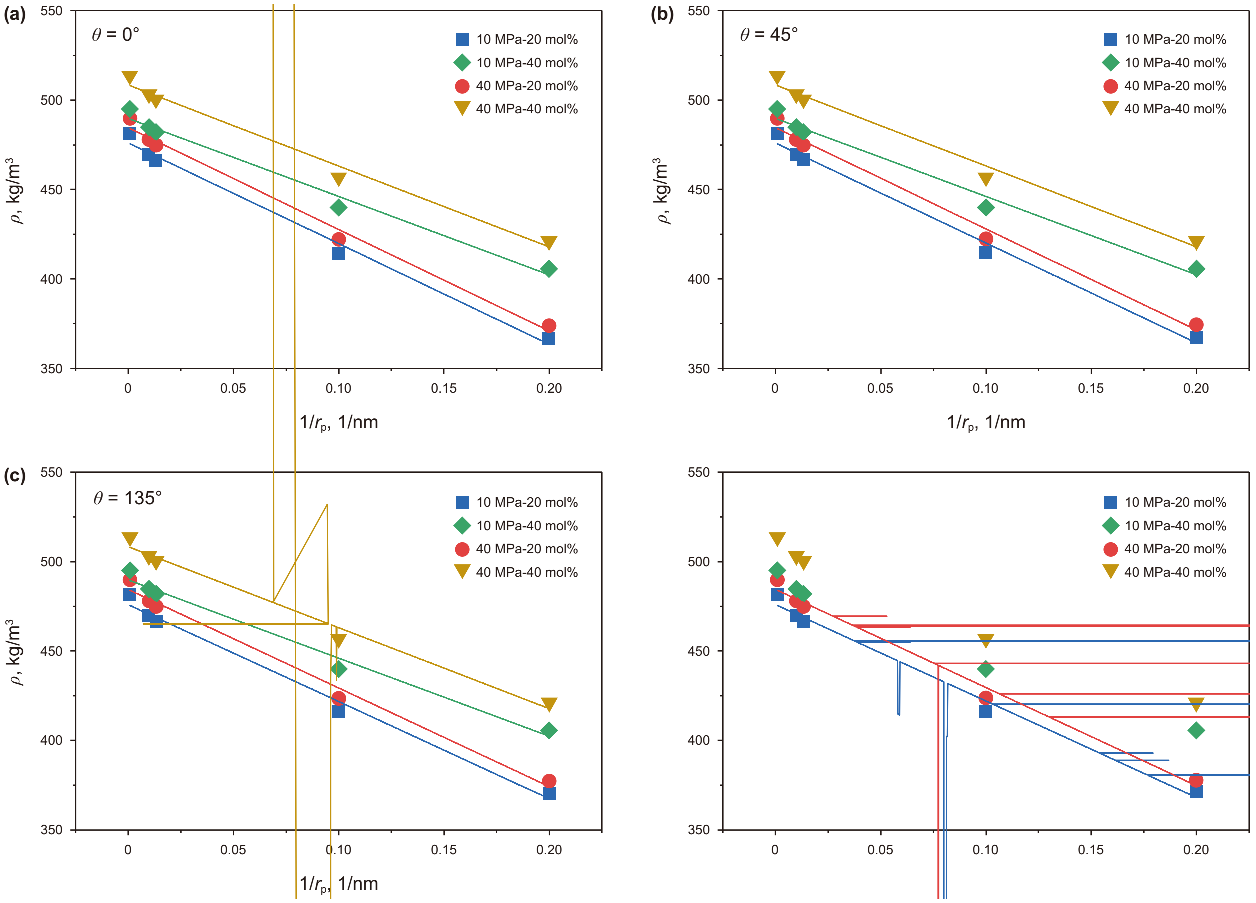

Fig. 11. Variation in oil density with pressure and CO_2 molar fraction across different pore sizes and wettability. **(a)** $\theta = 0^\circ$, **(b)** $\theta = 45^\circ$, **(c)** $\theta = 145^\circ$, **(d)** $\theta = 180^\circ$.

4.2.4. Minimum miscible pressure

MMP is a critical parameter in designing CO_2 injection strategies for shale oil formations. To evaluate the impact of nanoconfinement on the MMP of CO_2-oil in shale, this study systematically analyzes MMP variation with pore radius and hydrocarbon wettability. As shown in Fig. 13, nanoconfining effect markedly reduces the MMP (He et al., 2024; Wei et al., 2022; Wang et al., 2024). Specifically, as pore radius decreases from 100 to 5 nm, the MMP declines from 32.82 to 20.86 MPa, a reduction of 36.44%. When the pore radius ranges from 100 to 10000 nm, the MMP keeps relatively stable. However, below 100 nm, particularly under 75 nm, the MMP sharply declines with decreasing pore size, demonstrating a typical nanoconfining effect. This threshold aligns with trends observed for critical properties, saturation pressure, and other phase-related parameters as discussed earlier. Comparisons of the MMP–pore radius curves under different hydrocarbon wettability conditions ($\theta = 0^\circ$ and $\theta = 180^\circ$) nearly overlap, indicating that hydrocarbon wettability has negligible influence on the MMP of CO_2-oil in shale. This is because, under miscible conditions, the gas-liquid interface vanishes, causing capillary

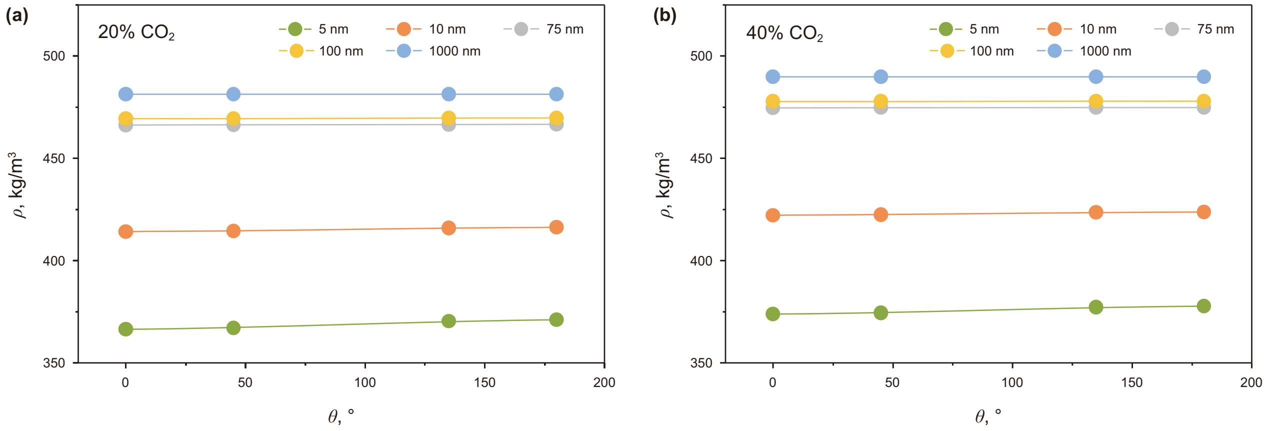

Fig. 12. Variation of oil density with CO_2 molar fraction for different pore sizes and hydrocarbon wettability under 10 MPa. **(a)** 20% CO_2, **(b)** 40% CO_2.

pressure to approach zero, thereby minimizing the impact of wettability on capillary pressure and miscibility. In conclusion, the MMP of the CO_2-oil in shale is significantly lower than that in conventional reservoirs, making CO_2 injection more likely to achieve miscibility in shale.

4.2.5. *Phase diagram*

This study explores the coupling effects of pore size and hydrocarbon wettability on the phase behavior of CO_2-oil in shale. It compares the impacts of different wettability conditions and CO_2 injection mole fractions on the *p*-*T* phase diagram under both bulk and 5 nm confinement conditions, as shown in Fig. 14. Under bulk conditions, increasing the CO_2 mole fraction leads to higher bubble point and critical pressures. In contrast, under confinement with a 5 nm pore radius and without capillary pressure, the *p*-*T* phase diagram shifts toward lower temperatures and pressures. The two-phase region becomes narrower, with the gas-liquid coexistence region contracting significantly. Additionally, both the critical temperature and pressure significantly decrease.

When capillary pressure is considered, the overall trend of the phase diagram remains unchanged, but the contraction of the phase envelope becomes more pronounced. As shown in Fig. 14(a), within 5 nm pores, capillary pressure further lowers the bubble point pressure, increases the upper dew point pressure, and decreases the lower dew point pressure. These changes lead to additional contraction of the two-phase region. At an extreme hydrocarbon-wetting condition ($\theta = 0^\circ$), the effect is more significant than that of non-wetting condition ($\theta = 180^\circ$). It indicates that stronger hydrocarbon wettability enhances capillary pressure and promotes the transition toward a single-phase region. This trend is consistently observed at both 20 mol% and 40 mol% of CO_2. Although hydrocarbon wettability markedly influences the shape of the phase envelope, it does not alter the position of the critical point. At the critical point, the properties of the gas and liquid phases converge, IFT approaches zero, and capillary pressure

IFT

the bulk saturation pressure. This delays the release of light components and enhances the dissolved gas-oil ratio during shale oil production. As pore size decreases and the system becomes increasingly hydrocarbon-wet, the P-T phase diagram further contracts, with a significantly narrowed two-phase region. These results indicate that phase behavior is synergistically governed by pore size and wettability.

5. Limitation

The model developed in this study provides a theoretical foundation for analyzing phase behavior in shale. However, it has certain limitations in two ways:

(1) Pore geometry assumption. A cylindrical pore is used for further calculation in this work. However, real shale formations contain irregular or slit-like pores, introducing potential deviations.
(2) Ideal fluid adsorption. In this work, adsorption is incorporated by modifying the V_m term in the PR-EOS and by adjusting the effective pore radius to reflect the presence of an adsorption layer. The thickness of this layer is estimated using an empirical correlation (Eq. (11)) based on the critical properties of each component. In practice, the thickness of the adsorption layer is also strongly influenced by pore wall wettability, which enhances fluid-wall interactions and promotes adsorption under highly oil-wet conditions. This effect is not fully captured in the current model, which may introduce bias in phase behavior predictions.

Our future work will focus on addressing these two limitations. Frist, take the pore geometry into account to characterize the effect of pore shape on phase behavior in shale. Meanwhile, establishing a quantitative relationship between hydrocarbon wettability, adsorption capacity, and adsorption layer thickness to improve the model's accuracy and applicability in complex shale systems.

6. Conclusion

The multi-phase interactions of CO_2-oil in shale were systematically investigated in this work. Special attention was given to the nanoconfined phase behavior with pore size, wettability and CO_2 molar fraction, including changes in critical properties, saturation pressure, oil density, MMP and *p-T* phase diagram. The implications of these shifts on fluid transport and CCUS-EOR were discussed in this paper. The main conclusions are as follows:

(1) The PR-EOS was modified to incorporate fluid-wall interactions and adsorption effects, and correlations for critical property shift were established based on existing experimental data. A unified VLE calculation model was developed to comprehensively account for fluid-wall interactions, fluid adsorption, capillary pressure, and wettability.
(2) The critical temperatures, critical pressures, saturation pressure, density, and MMP decrease with decreasing pore size, with more pronounced shifts observed below 75 nm. When the pore radius exceeds 75 nm, these parameters approach the bulk-phase values.
(3) The extent of critical property shifts correlates with carbon number, as heavier hydrocarbons exhibit greater shifts, critical pressure is more sensitive to nanoconfinement than critical temperature.
(4) Increased capillary pressure enriches light components in the liquid phase, reducing density and saturation pressure. Wettability further lowers bubble and upper dew point pressures while raising the lower dew point pressure, contracting the two-phase region. Stronger oil wettability causes greater shifts in the P-T phase diagram.

CRediT authorship contribution statement

Yu-Jiao He: Writing – original draft, Methodology, Investigation. **Bing Wei:** Writing – review & editing, Supervision, Resources, Project administration, Funding acquisition. **Jun-Yu You:** Writing – review & editing, Validation, Supervision, Methodology. **Le-Le Wang:** Writing – original draft, Methodology, Investigation. **Xiang Zhang:** Writing – original draft, Methodology, Investigation. **Han-Lin Luo:** Writing – original draft, Investigation. **Valeriy Kadet:** Writing – review & editing, Supervision, Conceptualization.

Declaration of competing interests

The authors declare that they have no known competing financial interests or personal relationships that could have appeared to influence the work reported in this paper.

Acknowledgments

The authors gratefully acknowledge financial support from the National Key Research and Development Program of China (2023YFE0120700), National Natural Science Foundation of China (52274041 and 52304023), Distinguished Young Sichuan Science Scholars (2023NSFSC1954). Natural Science Foundation of Chongqing (CSTB2022NSCQMSX0403).

Appendix A. Supplementary data

Supplementary data to this article can be found online at https://doi.org/10.1016/j.petsci.2025.12.005.

References

Adamson, A.W., Gast, A.P., 1967. Physical Chemistry of Surfaces. Interscience Publishers, New York.
Bocquet, L., Tabeling, P., 2014. Physics and technological aspects of nanofluidics. Lab Chip 14 (17), 3143–3158. https://doi.org/10.1039/C4LC00325J.
Cai, J., Qin, X., Xia, X., et al., 2024. Numerical modeling of multiphase flow in porous media considering micro- and nanoscale effects: a comprehensive review. Gas Sci. Eng. 131, 205441. https://doi.org/10.1016/j.jgsce.2024.205441.
Cho, H., Bartl, M.H., Deo, M., 2017. Bubble point measurements of hydrocarbon mixtures in mesoporous media. Energy Fuels 31 (4), 3436–3444. https://doi.org/10.1021/acs.energyfuels.6b02424.
Cui, X., Yang, E., Song, K., et al., 2018. Phase equilibrium of hydrocarbons confined in nanopores from a modified peng-robinson equation of state. In: SPE Annual Technical Conference and Exhibition. https://doi.org/10.2118/191547-MS.
Czarnota, R., Janiga, D., Stopa, J., et al., 2018. Acoustic investigation of CO_2 mass transfer into oil phase for vapor extraction process under reservoir conditions. Int. J. Heat Mass Tran. 127, 430–437. https://doi.org/10.1016/j.ijheatmasstransfer.2018.06.098.
Derouane, E.G., 2007. On the physical state of molecules in microporous solids. Microporous Mesoporous Mater. 104 (1–3), 46–51. https://doi.org/10.1016/j.micromeso.2007.01.003.
Dong, X., Xu, W., Liu, R., et al., 2022. Insights into adsorption and diffusion behavior of shale oil in slit nanopores: A molecular dynamics simulation study. J. Mol. Liq. 359, 119322. https://doi.org/10.1016/j.molliq.2022.119322.
Du, F., Huang, J., Chai, Z., et al., 2020. Effect of vertical heterogeneity and nanoconfinement on the recovery performance of oil-rich shale reservoir. Fuel 267, 117199. https://doi.org/10.1016/j.fuel.2020.117199.
Feng, D., Bakhshian, S., Wu, K., et al., 2021. Wettability effects on phase behavior and interfacial tension in shale nanopores. Fuel 290, 119983. https://doi.org/10.1016/j.fuel.2020.119983.
He, Y., Wei, B., Zhao, J., et al., 2024. Accurate determination of nano-confined minimum miscible pressure to aid CO_2 enhanced oil recovery and storage in

unconventional reservoirs. Adv. Geo-Energy Res. 12 (2), 141–155. https://doi.org/10.46690/ager.2024.05.06.

Ingebrigtsen, T.S., Dyre, J.C., 2014. The impact range for smooth wall-liquid interactions in nanoconfined liquids. Soft Matter 10 (24), 4324–4331. https://doi.org/10.1039/c3sm52441h.

Islam, A.W., Patzek, T.W., Sun, A.Y., 2015. Thermodynamics phase changes of nanopore fluids. J. Nat. Gas Sci. Eng. 25, 134–139. https://doi.org/10.1016/j.jngse.2015.04.035.

Jia, C., Zheng, M., Zhang, Y., 2014. Four important theoretical issues of unconventional petroleum geology. Acta Pet. Sin. 35 (1), 1–10 (in chinese). https://www.syxb-cps.com.cn/EN/10.7623/syxb201401001.

Lee, J.H., Lee, K.S., 2019. Investigation of asphaltene-derived formation damage and nano-confinement on the performance of CO_2 huff-n-puff in shale oil reservoirs. J. Pet. Sci. Eng. 182, 106304. https://doi.org/10.1016/j.petrol.2019.106304.

Li, M., Su, Y., Dong, M., et al., 2021. A numerical study of fluids desorption and phase behavior in shale oil reservoir using a chemical reaction model. J. Pet. Sci. Eng. 196, 108050. https://doi.org/10.1016/j.petrol.2020.108050.

Li, Q., Wang, Y., Wei, B., et al., 2024. Imbibition oil recovery from tight reservoir cores using microemulsion: Experiment and simulation. Capillarity 10 (2), 38–47. https://doi.org/10.46690/capi.2024.02.02.

Li, Z., Jin, Z., Firoozabadi, A., 2014. Phase behavior and adsorption of pure substances and mixtures and characterization in nanopore structures by density functional theory. SPE J. 19 (6), 1096–1109. https://doi.org/10.2118/169819-PA.

Lin, L., Babadagli, T., Li, A.H., 2025. An empirical model for predicting saturation pressure of pure hydrocarbons in nanopores. Fluid Phase Equilibr 588, 114232. https://doi.org/10.1016/j.fluid.2024.114232.

Peng, D.Y., Robinson, D.B., 1976. A new two-constant equation of state. Ind. Eng. Chem. Fundamen. 15 (1), 59–64. https://doi.org/10.1021/i160057a011.

Pitakbunkate, T., Balbuena, P.B., Moridis, G.J., et al., 2016. Effect of confinement on pressure/volume/temperature properties of hydrocarbons in shale reservoirs. SPE J. 21 (2), 621–634. https://doi.org/10.2118/170685-PA.

Rachford, J.H., Rice, J., 1952. Procedure for use of electronic digital computers in calculating flash vaporization hydrocarbon equilibrium. J. Pet. Technol. 4 (10), 19. https://doi.org/10.2118/952327-G.

Rui, Z., Deng, H., Hu, T., et al., 2025. Coupling mechanism analysis of CO_2 non-darcy flow in multi-scale reservoirs: A case study of the life-cycle process of fracturing-development in shale oil reservoirs. Pet. Sci. 22 (3), 1171–1199. https://doi.org/10.1016/j.petsci.2024.12.018.

Singh, S.K., Singh, J.K., 2011. Effect of pore morphology on vapor-liquid phase transition and crossover behavior of critical properties from 3D to 2D. Fluid Phase Equilibr 300 (1–2), 82–187. https://doi.org/10.1016/j.fluid.2010.10.014.

Soeder, D.J., 2018. The successful development of gas and oil resources from shales in North America. J. Petrol. Sci. Eng. 163, 399–420. https://doi.org/10.1016/j.petrol.2017.12.084.

Sobecki, N., Nieto-Draghi, C., Lella, A.D., et al., 2019. Phase behavior of hydrocarbons in nano-pores. Fluid Phase Equilibr 497, 104–121. https://doi.org/10.1016/j.fluid.2019.05.025.

Song, Z., Song, Y., Guo, J., et al., 2020. Adsorption induced critical shifts of confined fluids in shale nanopores. Chem. Eng. J. 385, 123837. https://doi.org/10.1016/j.cej.2019.123837.

Tan, S., Qiu, X., Dejam, M., et al., 2019. Critical point of fluid confined in nanopores: Experimental detection and measurement. J. Phys. Chem. C 123 (15), 9824–9830. https://doi.org/10.1021/acs.jpcc.9b00299.

Tao, L., Liu, W., Shi, J., et al., 2025. Experimental and theoretical determination of minimum miscibility pressure of supercritical CO_2 and alkanes at nano-confinement. Chem. Eng. Sci. 302, 120828. https://doi.org/10.1016/j.ces.2024.120828.

Tariq, Z., Estrada, J.K., Yan, B., et al., 2024. Numerical investigation of CO_2 solubility trapping mechanisms for enhanced storage in saline aquifers. Comput. Energy Sci. 1 (4), 175–187. https://doi.org/10.46690/compes.2024.04.03.

Teklu, T.W., Alharthy, N., Kazemi, H., et al., 2014. Phase behavior and minimum miscibility pressure in nanopores. SPE Res Eval. Eng. 17 (3), 396–403. https://doi.org/10.2118/168865-PA.

Travalloni, L., Castier, M., Tavares, F.W., 2014. Phase equilibrium of fluids confined in porous media from an extended Peng-Robinson equation of state. Fluid Phase Equilibr 362, 335–341. https://doi.org/10.1016/j.fluid.2013.10.049.

Vishnyakov, A., Piotrovskaya, E.M., Brodskaya, E.N., et al., 2001. Critical properties of Lennard-Jones fluids in narrow slit-shaped pores. Langmuir 17 (14), 4451–4458. https://doi.org/10.1021/la001641a.

Wang, G., Shen, R., Xiong, S., et al., 2025. Research progress on nano-confinement effects in unconventional oil and gas energy—With a major focus on shale reservoirs. Energies 18 (1), 166. https://doi.org/10.3390/en18010166.

Wang, S., Feng, Q., Javadpour, F., et al., 2015. Oil adsorption in shale nanopores and its effect on recoverable oil-in-place. Int. J. Coal Geol. 147, 9–24. https://doi.org/10.1016/j.coal.2015.06.002.

Wang, Y., Lei, Z., Sun, L., et al., 2024. Study on the minimum miscibility pressure and phase behavior of CO_2-shale oil in nanopores. Chem. Eng. J. 497, 154493. https://doi.org/10.1016/j.cej.2024.154493.

Wei, B., Zhong, M., Zhao, J., et al., 2022. Prediction method for the minimum miscibility pressure of crude oil and natural gas in micro-nano confined space. Acta Pet. Sin. 43 (11), 1604. https://www.syxb-cps.com.cn/CN/10.7623/syxb202211007.

Wei, J., Shang, D., Zhao, X., et al., 2024. Experimental study on production characteristics and enhanced oil recovery during imbibition and huff-n-puff injection in shale reservoir. Capillarity 12 (2), 41–56. https://doi.org/10.46690/capi.2024.08.02.

Weinaug, C.F., Katz, D.L., 1943. Surface tensions of methane-propane mixtures. Ind. Eng. Chem. 35 (2), 239–246. https://doi.org/10.1021/ie50398a028.

Wilson, G.M., 1969. A modified Redlich-Kwong equation of state, application to general physical data calculations. In: The 65th National Aiche Meeting.

Yang, G., Fan, Z., Li, X., 2019. Determination of confined fluid phase behavior using extended Peng-Robinson equation of state. Chem. Eng. J. 378, 122032. https://doi.org/10.1016/j.cej.2019.122032.

Yang, G., Li, X., 2020. Modified Peng-Robinson equation of state for CO_2/hydrocarbon systems within nanopores. J. Nat. Gas Sci. Eng. 84, 103700. https://doi.org/10.1016/j.jngse.2020.103700.

Yang, H., Jayaatmaja, K., Dejam, M., et al., 2022. Phase transition and criticality of methane confined in nanopores. Langmuir 38 (6), 2046–2054. https://doi.org/10.1021/acs.langmuir.1c02955.

Yang, Q., Sun, P., Fumagalli, L., et al., 2020. Capillary condensation under atomic-scale confinement. Nature 588 (7837), 250–253. https://doi.org/10.1038/s41586-020-2978-1.

Yarveicy, H., 2023. Effect of nanoparticles on phase behavior of surfactant-oil-water system: An application in multiphase flow system. Adv. Geo-Energy Res. 9 (3), 152–155. https://doi.org/10.46690/ager.2023.09.03.

Yuan, S., Han, H., Wang, H., et al., 2024. Research progress and potential of new enhanced oil recovery methods in oilfield development. Pet. Explor. Dev. 51 (4), 841–854. https://doi.org/10.1016/S1876-3804(24)60518-5 (in chinese).

Zarragoicoechea, G.J., Kuz, V.A., 2004. Critical shift of a confined fluid in a nanopore. Fluid Phase Equilibr 220 (1), 7–9. https://doi.org/10.1016/j.fluid.2004.02.014.

Zhang, K., Jia, N., Liu, L., 2018. Adsorption thicknesses of confined pure and mixing fluids in nanopores. Langmuir 34 (43), 12815–12826. https://doi.org/10.1021/acs.langmuir.8b02925.

Zhang, K., Jia, N., Liu, L., 2019. Generalized critical shifts of confined fluids in nanopores with adsorptions. Chem. Eng. J. 372, 809–814. https://doi.org/10.1016/j.cej.2019.04.198.

Zhang, Y., Lashgari, H.R., Di, Y., et al., 2017. Capillary pressure effect on phase behavior of CO_2/hydrocarbons in unconventional reservoirs. Fuel 197, 575–582. https://doi.org/10.1016/j.fuel.2017.02.021.

Zhao, J., Wang, L., Wei, B., et al., 2025. CO_2 utilization and geological storage in unconventional reservoirs after fracturing. Engineering 48, 92–106. https://doi.org/10.1016/j.eng.2025.01.005.

Zhao, R., Xue, H., Lu, S., et al., 2024. Molecular dynamics of quantitative evaluation of confined fluid behavior in nanopores media and the influencing mechanism: Pore size and pore geometry. Phys. Fluids 36, 092027. https://doi.org/10.1063/5.0226864.

Zheng, Z., Di, Y., Wu, Y., 2021. Nanopore confinement effect on the phase behavior of CO_2/hydrocarbons in tight oil reservoirs considering capillary pressure, fluid-wall interaction, and molecule adsorption. Geofluids 2021, 2435930. https://doi.org/10.1155/2021/2435930.

Zhong, J., Alibakhshi, M.A., Xie, Q., et al., 2020. Exploring anomalous fluid behavior at the nanoscale: direct visualization andquantification via nanofluidic devices. Acc. Chem. Res. 53 (2), 347–357. https://doi.org/10.1021/acs.accounts.9b00411.

Zhou, C., Pan, S., Jing, Z., et al., 2020. Shale oil and gas revolution and its impact. Acta Pet. Sin. 41 (1), 1–12. https://www.syxb-cps.com.cn/EN/10.7623/syxb202001001 (in chinese).

Zou, C., Tao, S., Hou, L., 2011. Unconventional Petroleum Geology. Geological Publishing House, Beijing.

Zuo, J., Guo, X., Liu, Y., et al., 2018. Impact of capillary pressure and nanopore confinement on phase behaviors of shale gas and oil. Energy Fuels 32 (4), 4705–4714. https://doi.org/10.1021/acs.energyfuels.7b03975.